Math. Model. Nat. Phenom. 20 (2025) 11
https://doi.org/10.1051/mmnp/2025002

Mathematical Modelling of Natural Phenomena
www.mmnp-journal.org

ACCURATE CEREBRAL VENOUS BLOOD FLOW SIMULATIONS COMPARED TO REAL DATA

Pierre Mollo[1,*], Guillaume Dollé[2], Olivier Balédent[3] and Stéphanie Salmon[2]

Abstract. In this work, we develop models of cerebral venous blood flows in realistic 3D geometries and run accurate numerical 3D simulations leveraging real data. These data come from Magnetic Resonance Imaging measures and provide both morphological and physiological information on the same subject. It allows to calibrate a subject specific simulation and improve its reliability. We present the complete pipeline going from data pre-processing to the integration in the simulation framework. The 3D Finite Element simulations in the main cerebral venous vessels are coupled with Windkessel reduced models, whose parameters are chosen according to the data, to take into account the neglected network. First results are discussed and compared with literature data, opening the way to obtain reliable information difficult or even impossible to obtain *in vivo* in a non-invasive way. All codes are in-house openly developed ones to ensure reproducibility.

Mathematics Subject Classification. 65N30, 76D05.

Received April 22, 2024. Accepted January 9, 2025.

1. Introduction

Progress in computational power and numerical methods has made possible complex bio-fluids simulations. The great interest of these numerical simulations is now obvious, as they give access to information difficult or even impossible to obtain *in vivo* in a non-invasive way. In particular, numerical simulations of blood flows in realistic geometries have been developed for years now by numerous teams: arterial blood flows were first considered [1–4] and more recently venous blood flows [5–9]. The venous network draining the blood from organs to the heart is less studied and though still less understood.

The main difficulty regarding the venous system is its rather high variability, even in healthy cases, making its responses to perturbations really individual-specific [10]. In addition, its interactions with other cerebral structures, such as the cerebro-spinal fluid (CSF), is crucial for proper function of the brain and yet complex since it implies local phenomena. The use of accurate 3D simulations with subject-specific data is then a possible way to observe these complex hemo-dynamics effects at specific points of interest. This motivates the development of procedures to extract real data and interface them with the numerical model. This work is a

Keywords and phrases: Computational fluid dynamic, cerebral venous blood flow, Navier-Stokes equations, fluid mechanics, finite element method, blood flows, Windkessel models.

[1] Centre for Analysis, Scientific Computing and Applications, TU Eindhoven, Eindhoven, The Netherlands.
[2] Laboratoire de Mathématiques de Reims, CNRS UMR 9008, URCA, Reims, France.
[3] CHIMERE, CNRS UR 7516, CHU Amiens, France.

* Corresponding author: p.m.mollo@tue.nl

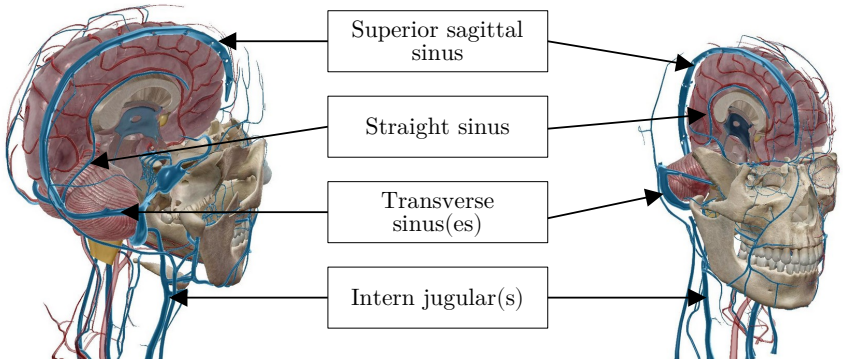

FIGURE 1. Atlas view of the intracranial compartment. (Images courtesy of Visible Body).

part of the project Human and Animal NUmerical Models for the crANio-spinal system (HANUMAN), in which several approaches are explored to study the whole craniospinal system. In this paper, we present a 3D numerical fluid model to compute blood flow in the cerebral venous network (CVN) which aims to integrate real data coming from magnetic resonance imaging (MRI) and phase contrast magnetic resonance imaging (PC-MRI) stored in the hyper intracranial pressure (HYPERPIC) database described hereafter. Numerical simulations are obtained *via* open access codes based on finite element method (FEM).

The whole structure composed by the brain, the spinal cord, the CSF compartments and the blood vasculature, forms the craniospinal system, a dynamic structure with many interactions. Since the skull is fully rigid in adults, a key parameter is the inner pressure of this system [11]. This intracranial pressure (ICP) corresponds to the overall CSF pressure and is influenced by the cerebral venous system, as developed in [12]. Indeed, the CVN is part of the glymphatic system, recently discovered, which plays a role in maintaining the homeostatic stability of the brain by exchanging proteins and extracting toxins [13]. These functions are ensured by close connection between the CVN and the CSF compartments, inducing a pressure relation. It follows that alterations of this CVN can play a role in many cerebral diseases as cerebral hypertension, multiple sclerosis, hydrocephalus, Alzheimer's and other neuro-degenerative diseases. In presence of stenosis, it has been showed that it can also induce inconvenience such as tinnitus [8]. Numerical simulations involving computational fluid dynamics (CFD) can provide information concerning the pressure. In particular, ICP measurements are not carried out on healthy subjects and consequently, simulations can give insights in deregulation of the system, leading then to pathologies. In addition, the complete knowledge of the associated velocity field allows to derive any quantities of interest, including wall shear stress or oscillatory indexes, depending on the clinical needs. For all these reasons, developing a 3D numerical model of the CVN interfaced with real data seems to be a valuable first step to better understand the complex interactions between blood and CSF flows.

The CVN is composed of veins and sinuses, they both drain venous blood from the brain to the heart, but they differ in their composition. On the one hand, veins are blood vessels in the usual sense since they are blood *pipes* composed by three layers (*intima*, *media*, *adventice*). The distribution and composition of these layers gives veins flexibility and elasticity [14] and makes them sensitive to pressure variation. On the other hand, sinuses are cavities formed by folds of the dura mater, a dense membrane surrounding the brain, conferring them a quasi-rigid structure. It follows that, in opposition to veins, sinuses are almost insensitive to pressure variation over short time period like cardiac cycle, but they remain plastic in long-term constraint. The sinuses are inherent to the cranial compartment and their properties hold until they flow out of the skull into the internal jugulars, the delimitation is highlighted in Figure 2d. In this study, we choose to focus on the main CVN composed by: the superior sagittal sinus, the straight sinus, the two lateral transverse and sigmoid sinuses. A part of the internal jugulars is also kept in the model to ensure coherence of the upstream flow although they do not respect the rigid wall assumption. An atlas representation of this main CVN is shown in Figure 1. This focus on sinuses allows to neglect the possible fluid-structure interactions and makes the

model computationally tractable. However, this approach excludes the peripheral venous network, which can nevertheless be significant depending on individuals. This choice is first motivated by the technical limitations induced by PC-MRI regarding the size of the vessels composing this peripheral network, but also by the position in the MRI machine. Indeed, during the acquisitions the subjects are in the supine position where venous blood is essentially drained by jugulars. The peripheral network draining the blood in standing and sitting positions is thus almost invisible in MRI images [15].

This document is organized as follows. The first section is dedicated to the treatment of the data; from the extraction to the interface with the numerical model considered in the second section. In the third section, numerical results are presented and discussed. Conclusion and perspectives opened by this work can be found in the last section.

2. Methodology for MRI processing

2.1. Materials and data

The CHIMERE team from Amiens CHU is a HANUMAN project partner specialized in MRI acquisitions. The team carried out a study named HYPERPIC to understand how CSF, arterial and venous flows interact with ICP. To do so, they measure by PC-MRI flow curves synchronized with cardiac cycle at different locations of the craniospinal system in healthy volunteers and patients suspected to present high ICP. Pressure measurements are obtained from lumbar puncture and are therefore not allowed for healthy subjects. This study was approved by an independent ethic committee and a description of the data is detailed in the literature [16]. In this study, 16 healthy subjects, half men and women, are considered with no neurological or spinal disease known *a priori*. The protocol of this study includes morphological MRI sequences and PC-MRI measurements. Our goal is then to use both geometrical and physiological information as inputs of our *in silico* fluid models.

The MRI acquisitions are fast, noninvasive and nonirradiating imaging techniques, providing a 3D angiography of the intracranial and cervical vasculature. The images were acquired on 3T scanner (Philips Achieva). 3D MRI angio images provides good structural information with a millimeter scale space resolution in the acquisition plane. Capturing a fine blood vessel structure from the MRI is crucial since the precision of FEM simulations relies on a good representation of the vessel physical boundary. Among the available series in the HYPERPIC MRI datasets, maximum intensity project (MIPs) series were selected for having a fine grained space resolution. These series have also good properties adapted to depict small vessels [17], the contrast being sufficiently high compared to surrounding structures. The settings is the following: the MIPs series are acquired in the axial plane with a resolution of $288 \times 288 \times 80$ for a spacing of $0.76 \times 0.76 \times 2.94$ (mm^3).

The PC-MRI acquisitions complete the structural information by quantifying the dynamic inside slices of interest. In particular, it gives access to the magnitude of the blood velocity at specific locations of the CVN. A PC-MRI slice is composed of a volumetric grid with some spacial resolution and the velocity is recorded following a prescribed velocity encoding. The amplitude of the fluid velocity is recorded on each voxel of the grid in the direction $\mathbf{d}$ normal to the slice S. Each slice gives a time dependant velocity map with a duration of one cardiac cycle split in 32 time steps. To do so the PC-MRI acquisition is synchronized on the cardiac frequency. The final result is a mean cardiac cycle produced by average of 256 cardiac cycles recordings. To optimize the quality of the PC-MRI, the velocity encoding must be selected in a range close to the maximum expected velocity of the fluid of interest. The acquisition error is below 10% and is sufficient to give a valuable information on fluid flows in a non-invasive way and can be done in a clinical routine [18].

As the cranio-spinal system is very variable, the main objective of this work is to provide a complete pipeline versatile enough to be able to take into account specific data from subjects. Then, we have decided to consider only healthy subjects of the cohort.

However, even in healthy cases, the overall form of the CVN is subject to inter-individual variation. In particular, the sinus confluence configuration (SCC) formed by the connection of the superior sagittal sinus (SSS) and the straight sinus (StS) to the right transverse sinus (RTS) and left transverse sinus (LTS) can follow several paths. Studies on the distribution of the SCC form in healthy population have been made in [19] and

more recently in [20, 21]. Among the 16 healthy participants available in the HYPERPIC dataset, two subjects have been selected for their distinct SCC illustrated in Figures 10 and 11 from numerical results in Section 4. They have been selected as they are representative of the main encountered paths. The T2 case (Fig. 10) is characterized by a fully connected sinus tree made of the SSS, the StS, the LTS and the RTS up to the jugulars; the T6 case (Fig. 11) has a splitted network with two parts: couple {SSS,RTS} on the one hand, and {LTS,StS} on the other.

2.2. Morphological extraction of vessels

Meshing the geometry of the vessels of interest is required to proceed with the CFD simulations. Virtual Angiography Toolkit (AngioTK)[1] is a framework developed in a former project implementing a full pipeline from the original MRI to a virtual MRI generated from CFD simulation using a set of numerical tools [22]. Some of these tools were used in this work to extract the morphology of the vessels. The process is summed up in the following steps:

(i.) Filter the MRI properly to remove undesired structures and noise.
(ii.) Parcelize to build a binary voxel map and highlight vessels of interest.
(iii.) Skeletonize the binary map to extract centerlines with a radius information.
(iv.) Reconstruct a smooth closed surface extrapolated from the centerlines properties with cutted ends.
(v.) Reconstruct a volumetric mesh adapted to the FEM simulations.

The first image pre-processing step (i) improves the MRI image by filtering the noise and removing undesired elements from the 3D voxel matrix. Many algorithms may be used to highlight vessels with more or less efficiency and the choice of the filtering method depends inherently on the acquisition modality. Ranking Orientation Responses of Path Openings (RORPO)[2] is an in-house vesselness filtering tool developed during a former work [23] that has been used to extract the HYPERPIC sinuses network. The particularity of this method is to take into account morphological information by removing non-tubular structures during the process. RORPO has demonstrated its ability to achieve good results when compared to the state of the art methods despite having a high memory cost with respect to the image resolution [24].

The image segmentation steps (ii) is performed using classical algorithms available in the *3D slicer* software (thresholding, *etc.*) [25]. Only vessels of interest are kept to reduce the global computation cost. This step requires a special attention since under- or over- segmentation would result in vessel disconnections or merges (*e.g.* arteries close to jugulars).

The center lines extraction step (iii) uses a type of skeletonization algorithm based on Voronoi diagrams implemented in the VMTK library [26, 27]. This method encodes the geometry as a 1D line (see Fig. 2c) formed by set of nodes located at the centers of the Voronoi diagram (approximately at the center of the vessel). A local size metric is calculated as the maximum radius of the inscribed sphere along the local vessel. The centerline is deduced from the shortest path in the diagram connecting the ends of the vessel branches. The geometry precision depends inherently on the quality of the binary map, but also on the MRI acquisition that must depict the vessels boundary correctly. The characteristic radii of our vessels of interest obtained after the center lines extraction, showed in Figure 2c, is comparable to the values found in the study [28]. The detailed comparison is presented in Table 1 for our selected subjects T2 and T6.

For the final steps (iv) and (v), a surface is reconstructed from the centerlines using a levelset method with a marching cube algorithm and smoothed using a Taubin method [29]. The 3D frontal Delaunay mesh is generated from the surface using an open source 3D finite element mesh generator with CAD support (GMSH [30]) and adapted using an open source software for simplicial remeshing (MMG3D [31–33]). An illustration of the mesh obtained at the end of the process is presented in Figure 2d. The limitations inherent to this approach are further discussed in the Section 4.3.

[1] https://github.com/vivabrain/angiotk
[2] https://github.com/path-openings/RORPO

TABLE 1. Veins characteristic radii in (mm).

	Radius (mm)		
Vessel	[28]	T2	T6
Superior sagittal sinus	$2.0 \rightarrow 3.19$	4.64 ± 0.23	2.95 ± 0.18
Straight sinus	2.5	2.31 ± 0.86	1.76 ± 0.29
Right transverse sinus	$1.78 \rightarrow 2.52$	3.15 ± 0.37	2.27 ± 0.45
Left transverse sinus	$3.09 \rightarrow 4.37$	4.29 ± 0.42	3.00 ± 0.30
Right internal jugular	$2.52 \rightarrow 3.99$	4.44 ± 0.37	2.86 ± 0.34
Left internal jugular	$3.9 \rightarrow 6.18$	3.23 ± 0.62	3.07 ± 0.55

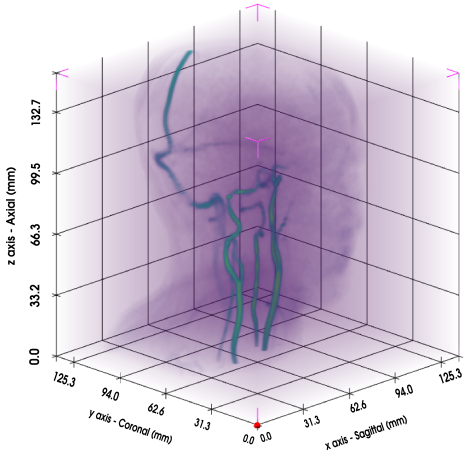

(a) MRI volume representation.

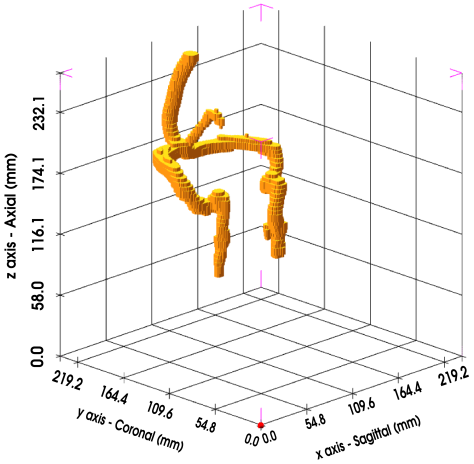

(b) Binary segmentation.

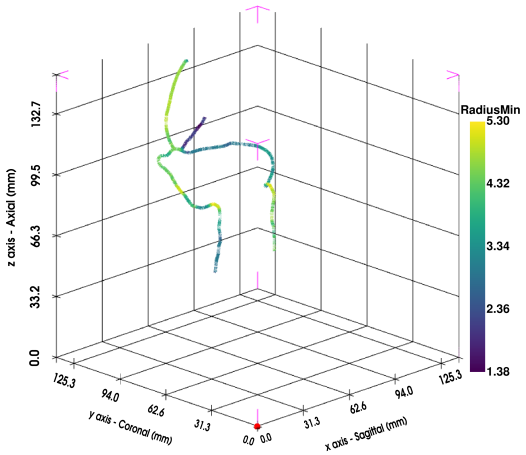

(c) Computed centerlines.

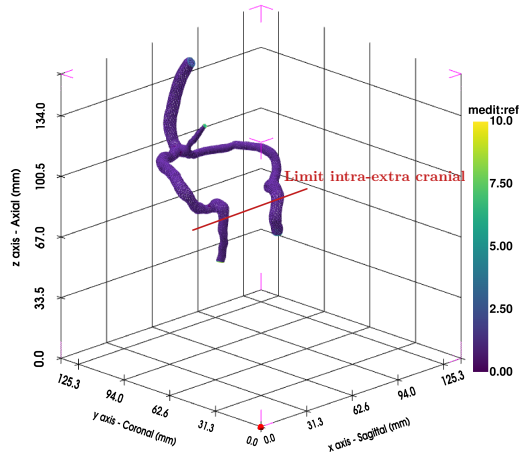

(d) Smooth surface mesh.

FIGURE 2. Subject T2 surface mesh extrapolated from 3D segmentation through 1D centerlines with estimated nodal radius.

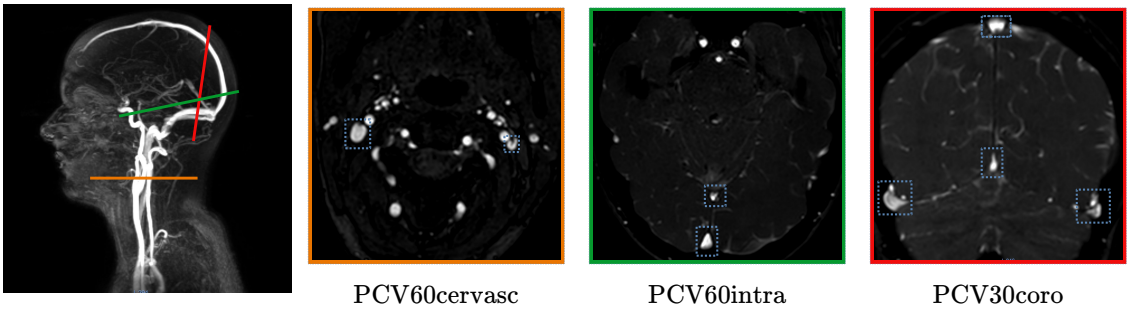

FIGURE 3. Location of the PC-MRI slices for T2 and the corresponding amplitude images.

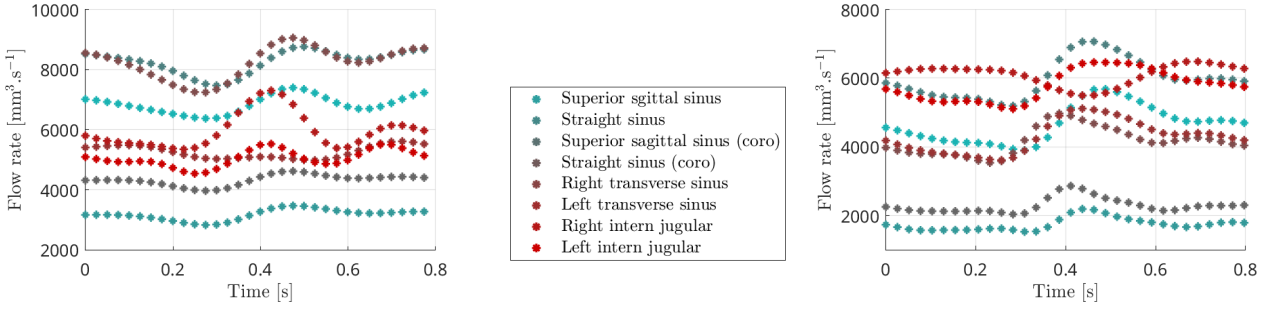

(a) T2 flow rates.

(b) T6 flow rates.

FIGURE 4. Raw flow rates obtained after the processing of the PC-MRI acquisitions.

2.3. Flow rate extraction from PC-MRI

In our context, we have 3 PC-MRI slices per subject at our disposal. Their locations are illustrated in Figure 3 for the subject T2 and are approximately the same for all the cohort. These slices are: (1) *PCV30coro* with a coronal orientation, $1 \times 1 \times 3$(mm) resolution and $300(\mathrm{mm\,s^{-1}})$ encoding, located at the back of the head. It intersects the superior sagittal sinus, the straight sinus and both transverse sinuses. (2) *PCV60intra* with a transverse orientation, $1 \times 1 \times 2$(mm) resolution and $600(\mathrm{mm\,s^{-1}})$ encoding. This one is located above the transverse sinuses and intersects the straight and the superior sagittal sinuses. (3) *PCV60cervasc* with a transverse orientation, $1 \times 1 \times 2$(mm) resolution and $600(\mathrm{mm\,s^{-1}})$ encoding. This last one is located above the cervical level and intersects internal jugulars. It follows that we have access to 8 sections of the CVN.

The software *Flow* [34] is used to segment, integrate and convert the velocity maps coming from the PC-MRI acquisitions into flow rates. Since the flow rates obtained depend on the segmentation defined by the user, we consider several different segmentations and compute an effective signal using Gaussian process regression. This serves to mitigate the introduction of user-dependent error. The effective flow rates we obtain following this process are presented in Figure 4. The data provided are averaged over 256 cardiac cycles during the acquisition phase. Indeed, since flow rates are influenced by numerous causes, it is necessary to work with a mean cycle to be representative. In Table 2, we compare our measurements to a study made by Stoquart-ElSankari *et al.* [10] gathering data from 18 healthy individuals. We then observe that all the raw flows for our subject T2 and T6 are in the ranges provided by the study. We also remark that a zero flux in some vessels can appear in the ranges from [10], it actually happens that all the blood is drained by only one side without being a pathological situation.

TABLE 2. Flow rates are given in ($mm^3\,s^{-1}$). Results of venous blood flow in 18 healthy volunteers, from study [10].

	Reference		T2		T6	
Location	Range	Mean ± s.d.	Mean	Rescale	Mean	Rescale
Right internal jugular	$0 \to 11\,350$	6650 ± 2383	5965	7295	6097	4341
Left internal jugular	$0 \to 9084$	2683 ± 2500	5052	6177	5787	4120
Outflow (sum)			11 017	13 472	11 884	8461
Sup. sagittal sinus	$4350 \to 7100$	5917 ± 950	6840	9203	4662	6156
Straight sinus	$1483 \to 2983$	2033 ± 467	3172	4269	1746	2305
Inflow (sum)			10 012	13 472	6408	8461
Right transverse sinus	$1550 \to 13\,600$	7233 ± 3400	8219	8219	4165	4164
Left transverse sinus	$0 \to 7767$	3250 ± 2533	5253	5253	4296	4296
Outflow (sum)			13 472	13 472	8461	8461

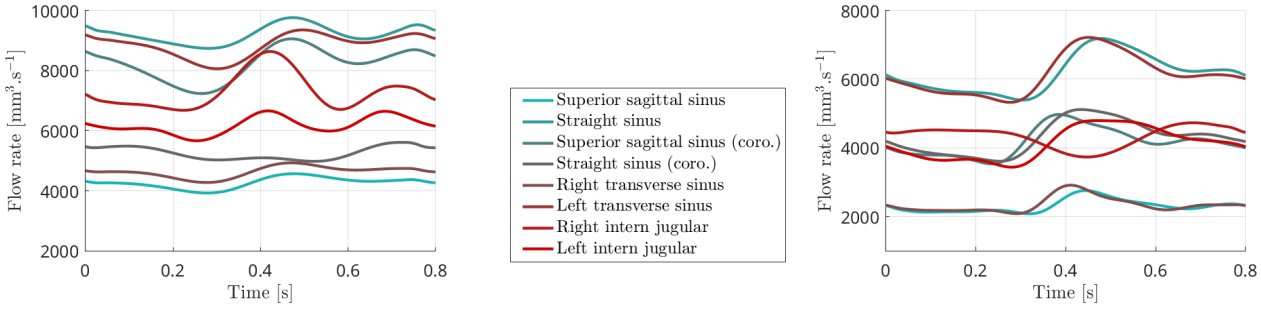

(a) T2 flow rates.

(b) T6 flow rates.

FIGURE 5. Flow rates after interpolation by splines and rescaling.

In order to be integrated in the numerical model, these raw flow rates have to be processed. Since we will assume in Section 3 that the fluid is incompressible and that the domain is rigid, we must ensure that the volume of fluid entering in the system is equal to the exiting volume. In our case, the sum of blood volume passing through the superior sagittal sinus and the straight sinus should be equal to the sum of blood volume passing through the internal jugulars. To make data compatible to our assumptions, we proceed to a rescaling of flow rates. To circumvent the effect of individual variability, we first define vessel groups: the SSS with the StS, the RTS with the LTS and the internal jugulars together. We then assume that these three groups have the same blood volume flowing through them over a cardiac cycle. These volumes are computed by integration of the corresponding flow rates over a cardiac cycle duration. The volume of the transverse sinuses group is chosen as reference, since its acquisition is more accurate, and the other volumes are adjusted to match it. The ratio between vessels inside each group is conserved while adjusting the total volume. The flow rates obtained after rescaling are presented in Figure 5 and correspond to the actual inputs of the model. After this rescaling procedure, we observe that the flow rates of the SSS and StS are higher than the ranges provided by literature, see Table 2. This is due to current limitation of our approach where several vessels are neglected, meaning that we are not able to capture all the entering blood volume. The rescaling choice is motivated by our desire to keep the exiting flow rates as close to acquisitions as possible. In particular, we only modify here the mean flow rates of vessels that will be used as inlets, while the flow ratio between them and the shape of the flow rates are

preserved. The transverse sinuses flow rates are not modified as they will be used as a ground-truth to adjust the model parameters.

3. Numerical model

3.1. Fluid modelling

The blood volume is mainly composed of plasma (54%) and red cells (45%), where the plasma is itself essentially composed of water (97%). Despite its non-Newtonian intrinsic nature induced by cells suspension, the blood can be considered homogeneous when observed on a macroscopic scale ($\geq$ (mm)). In addition, in the vascular structures we investigate, *i.e.* medium/large vessels, the blood is always in motion and red cells are not able to form rouleau. These remarks allow us to consider the blood as: (1) incompressible, (2) homogeneous, (3) Newtonian, and (4) isothermal [35, 36]. The set of incompressible Navier-Stokes equations is the usual candidate to describe the dynamic of such type of fluid. In the Eulerian description the fluid motion is encoded by a vectorial velocity field denoted $\mathbf{u}$ and a scalar pressure field denoted p. A fluid is also characterized by its density ρ, which remains constant in the particular case of incompressible homogeneous fluid, and its dynamic viscosity η. Although the rheology of blood depends on several factors (*e.g.* protein concentration, cell deformability, shear field [37]) and causes uncertainty in the choice of ρ and η, their ranges remain reduced and allow us to consider fixed reference values $\rho = 1.05 \times 10^{-6}(\mathrm{kg\,mm^{-3}})$, $\eta = 3.5 \times 10^{-6}(\mathrm{kg\,mm^{-1}\,s^{-1}})$ [6].

Using the above notations, we can introduce the Navier–Stokes system of equations. Let $[0, T]$ and $\Omega \subset \mathbb{R}^d$ be the time interval and the domain of interest with $d = 3$ the dimension. We denote $\Gamma = \partial\Omega$ its boundary and we assume that it exists a partition $\Gamma = \Gamma_{\mathrm{Dir}} \cup \Gamma_{\mathrm{Neu}}$. This partition is such that $\Gamma_{\mathrm{Dir}} \cap \Gamma_{\mathrm{Neu}} = \emptyset$ and $\Gamma_{\mathrm{Neu}} \neq \emptyset$. The problem reads

$$
\begin{cases}
\rho\dfrac{\partial \mathbf{u}}{\partial t} + \rho(\mathbf{u}\cdot\nabla)\mathbf{u} - \eta\Delta\mathbf{u} + \nabla p = \mathbf{f} & \text{in } [0,T]\times\Omega & \text{(3.1a)}\\
\nabla\cdot\mathbf{u} = 0 & \text{in } [0,T]\times\Omega & \text{(3.1b)}\\
\mathbf{u} = \mathbf{g} & \text{on } [0,T]\times\Gamma_{\mathrm{Dir}} & \text{(3.1c)}\\
\eta\dfrac{\partial \mathbf{u}}{\partial \mathbf{n}} - p\mathbf{n} = P\mathbf{n} & \text{on } [0,T]\times\Gamma_{\mathrm{Neu}} & \text{(3.1d)}\\
\mathbf{u} = \mathbf{u}_0 & \text{in } \{0\}\times\Omega & \text{(3.1e)}\\
p = p_0 & \text{in } \{0\}\times\Omega & \text{(3.1f)}
\end{cases}
$$

where $\mathbf{n}$ is the outer unit normal to the boundary, $\mathbf{f}$ represents the external forces, $\mathbf{g}$ is a prescribed boundary conditions and P is the external pressure. The first equation (3.1a) comes from the conservation of the momentum and the second one (3.1b) from the incompressibility hypothesis. The equation (3.1c) is a Dirichlet boundary condition, it is used to model either vessel walls in the homogeneous case (*i.e.* $\mathbf{u} = 0$) and the inlets by imposing the velocity corresponding to the flow rates computed in Section 2.3. The equation (3.1d) is a generalized Neumann boundary condition used to couple the 3D model with the Windkessel reduced model *via* the external pressure term P found at the outlet level. Indeed, by restricting ourselves to the intracranial compartment, we neglect the downstream part of the network. These Neumann conditions allow us to take this part into account in the model by mimicking its effect on the flow. The last two equations (3.1e) and (3.1f) correspond to the initial state of the system and is computed by solving the steady-state Stokes equations (linearized version of Navier–Stokes). Gravity is neglected here, leading to $\mathbf{f} = 0$.

We introduce the functional spaces $V = \{\mathbf{v} \in (H^1(\Omega))^d, \mathbf{v}_{|\Gamma_{\mathrm{Dir}}} = \mathbf{0}\}$ for the velocity and $Q = L^2(\Omega)$ for the pressure. These functional spaces are equipped with inner products $\langle \mathbf{u}, \mathbf{v}\rangle_V = \int_\Omega \mathbf{u}\cdot\mathbf{v} + \nabla\mathbf{u} : \nabla\mathbf{v}\ \mathrm{d}x$ and $\langle p, q\rangle_Q = \int_\Omega pq\ \mathrm{d}x$, and the associated norms $\|\mathbf{v}\|_V = \sqrt{\langle \mathbf{v}, \mathbf{v}\rangle_V}$ and $\|q\|_Q = \sqrt{\langle q, q\rangle_Q}$. Where : denotes the

contracted product of derivatives

$$\nabla \mathbf{u} : \nabla \mathbf{v} = \sum_{i=1}^{d} \sum_{j=1}^{d} \sum_{k=1}^{d} \frac{\partial u_i}{\partial x_j} \frac{\partial v_i}{\partial x_k}.$$

For $t \in [0, T]$, multiplying (3.1a) by a test function $\mathbf{v} \in V$ and integrating it, we obtain

$$\int_{\Omega} \frac{\partial \mathbf{u}}{\partial t} \cdot \mathbf{v} + (\mathbf{u} \cdot \nabla)\mathbf{u} \cdot \mathbf{v} - \nu \Delta \mathbf{u} \cdot \mathbf{v} + \nabla p \cdot \mathbf{v} \, \mathrm{d}x = 0, \tag{3.2}$$

then invoking the Green's and the Stokes formulas, and using the boundary conditions coming from (3.1c) and (3.1d), leads to the weak form

$$\int_{\Omega} \frac{\partial \mathbf{u}}{\partial t} \cdot \mathbf{v} + (\mathbf{u} \cdot \nabla)\mathbf{u} \cdot \mathbf{v} - \nu \nabla \mathbf{u} : \nabla \mathbf{v} + p(\nabla \cdot \mathbf{v}) \, \mathrm{d}x = \int_{\Gamma_{\mathrm{Neu}}} P\mathbf{n} \cdot \mathbf{v} \, \mathrm{d}\sigma. \tag{3.3}$$

If we now look at (3.1b), coming from the incompressible hypothesis, we multiply it by a test function $q \in Q$ and we integrate over the domain, we obtain:

$$\int_{\Omega} q(\nabla \cdot \mathbf{u}) \, \mathrm{d}x = 0. \tag{3.4}$$

To solve these nonlinear equations, we consider the characteristics method introduced in [38]. This linearization method leads to a generalized unsteady Stokes problem and can be considered as an implicit approximation, it then gives an unconditionally stable scheme [39]. For $K \in \mathbb{N}$, $\delta t = T/K$ denotes the time step used to discretize the time interval and we denote $t^{(k)} = k\delta t$, $\mathbf{u}^{(k)} = \mathbf{u}(t^{(k)}, .)$ and $p^{(k)} = p(t^{(k)}, .)$. We also need to introduce $\mathbf{X}\left(t^{(k)}\right)$, the position at $t^{(k)}$ of the particle which is in $\mathbf{X}\left(t^{(k+1)}\right)$ at $t^{(k+1)}$ coming from the characteristics method. The time scheme chosen is here an Euler scheme which limits the time convergence rate to 1. Injecting the time discretization in (3.3) gives

$$\int_{\Omega} \frac{1}{\delta t} \mathbf{u}^{(k+1)} \cdot \mathbf{v} - \nu \nabla \mathbf{u}^{(k+1)} : \nabla \mathbf{v} + p^{(k+1)}(\nabla \cdot \mathbf{v}) \, \mathrm{d}x = \int_{\Omega} \frac{1}{\delta t} \left(\mathbf{u}^{(k)} \circ \mathbf{X}^{(k)} \right) \cdot \mathbf{v} + \int_{\Gamma_{\mathrm{Neu}}} P^{(k+1)} \mathbf{n} \cdot \mathbf{v} \, \mathrm{d}\sigma. \tag{3.5}$$

As detailed in the following Section 3.2, the output $P^{(k+1)}$ of the Windkessel model is a function of the current and previous velocity states, it then reads $P^{(k+1)} = P\left(\{\mathbf{u}^{(i)}\}_{i=0}^{k+1}\right)$. We split (3.5) in several terms denoted:

$$a(\mathbf{u}, \mathbf{v}) = \int_{\Omega} \nu \nabla \mathbf{u} : \nabla \mathbf{v} \, \mathrm{d}x, \tag{3.6}$$

$$b(p, \mathbf{v}) = -\int_{\Omega} p(\nabla \cdot \mathbf{v}) \, \mathrm{d}x, \tag{3.7}$$

$$c(\mathbf{u}, \mathbf{v}) = \int_{\Omega} \frac{1}{\delta t} \mathbf{u} \cdot \mathbf{v} \, \mathrm{d}x, \tag{3.8}$$

$$d(\mathbf{u}, \mathbf{v}) = \int_{\Gamma_{\mathrm{Neu}}} P\left(\{\mathbf{u}^{(i)}\}_{i=0}^{k+1}\right) \mathbf{n} \cdot \mathbf{v} \, \mathrm{d}\sigma, \tag{3.9}$$

In this way, the associated variational problem reads: knowing $(\mathbf{u}^{(k)}, p^{(k)})$, find $(\mathbf{u}^{(k+1)}, p^{(k+1)}) \in V \times Q$ such that

$$\begin{cases} c\left(\mathbf{u}^{(k+1)}, \mathbf{v}\right) + a\left(\mathbf{u}^{(k+1)}, \mathbf{v}\right) + b\left(p^{(k+1)}, \mathbf{v}\right) + d(\mathbf{u}^{(k+1)}, \mathbf{v}) = c\left(\mathbf{u}^{(k)} \circ \mathbf{X}^{(k)}, \mathbf{v}\right) & \mathbf{v} \in V \\ b\left(q, \mathbf{u}^{(k+1)}\right) = 0 & q \in Q \end{cases}. \tag{3.10}$$

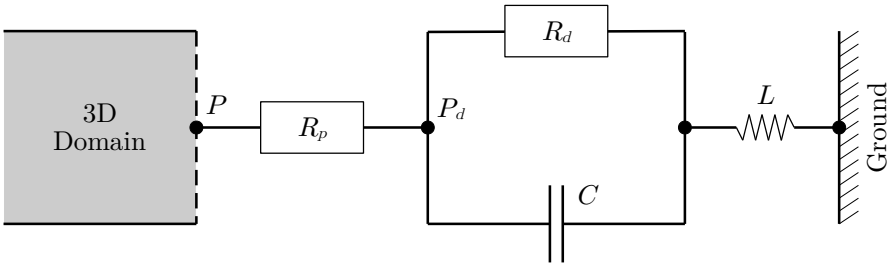

FIGURE 6. Representation of the four components Windkessel model.

3.2. Windkessel four-components boundary condition

To take into account the truncated part of the network, we interface a Windkessel model to the non-homogeneous Neumann boundary condition in (3.1d), through the external pressure P. Different 0D models exist to model vascular networks and give a variety of behavior for P. However, using complex 0D models usually involves more parameters and can make the model tuning intractable. In this paper, we use at each outlet a four components Windkessel model composed by; two resistances R_p (proximal) and R_d (distal), a capacitor C and a coil L. The resistances are used to encode the hydraulic resistance applied by the vascular network, while the capacitor models its compliance (elasticity) and the coil models the fluid inertia.

The generic circuit used for the four components model is depicted in Figure 6 and has the following exact solution [40]

$$P(t) = P(0)\mathrm{e}^{\frac{-t}{R_dC}} + L\left(Q'(t) - Q'(0)\mathrm{e}^{\frac{-t}{R_dC}}\right) + R_p\left(Q(t) - Q(0)\mathrm{e}^{\frac{-t}{R_dC}}\right) + \frac{1}{C}\int_0^t Q(s)\mathrm{e}^{\frac{s-t}{R_dC}}\,\mathrm{d}s, \tag{3.11}$$

where $Q(t) = \int_\gamma \mathbf{u}(t)\,\mathrm{d}\sigma$ and γ denotes the outlet surface. Using the time discretization, the integral part of equation can be approximated by a trapezoidal rule

$$\int_{t^{(0)}=0}^{t^{(k)}=t} Q(s)\mathrm{e}^{\frac{s-t^{(k)}}{R_dC}}\,\mathrm{d}s \simeq \frac{\delta t}{2}Q^{(0)}\mathrm{e}^{\frac{-t^{(k)}}{R_dC}} + \delta t\sum_{j=1}^{k-1} Q^{(j)}\mathrm{e}^{\frac{(j-k)\delta t}{R_dC}} + \frac{\delta t}{2}Q^{(k)}. \tag{3.12}$$

Invoking again the time discretization, a backward Euler's scheme allows to obtain an approximation of the flow rate derivative, it reads

$$Q'^{(k)} \simeq \frac{Q^{(k)} - Q^{(k-1)}}{\delta t}. \tag{3.13}$$

Given an estimation $\hat{Q}'^{(0)}$ of $Q'^{(0)}$ that exponentially vanishes over the time, we obtain the scheme

$$\begin{aligned} P^{(k)} = {} & P^{(0)}\mathrm{e}^{\frac{-t^{(k)}}{R_dC}} + L\left(\frac{Q^{(k)} - Q^{(k-1)}}{\delta t} - \hat{Q}'^{(0)}\mathrm{e}^{\frac{-t^{(k)}}{R_dC}}\right) + R_p\left(Q^{(k)} - Q^{(0)}\mathrm{e}^{\frac{-t^{(k)}}{R_dC}}\right) \\ & + \frac{\delta t}{2C}\left(Q^{(0)}\mathrm{e}^{\frac{-t^{(k)}}{R_dC}} + 2\sum_{j=1}^{k-1} Q^{(j)}\mathrm{e}^{\frac{(j-k)\delta t}{R_dC}} + Q^{(k)}\right). \end{aligned} \tag{3.14}$$

Let $R_{\text{eq}} = R_p + R_d$ be the equivalent resistance of the model, we set $P^{(0)} = Q^{(0)} R_{\text{eq}}$ for the initial pressure and $\hat{Q}'^{(0)} = 0$ as the initial flow rate derivative. The scheme obtained

$$P^{(k)} = Q^{(0)} \mathrm{e}^{\frac{-t^{(k)}}{R_d C}} \left(\frac{\delta t}{2C} + R_d \right) + \frac{\delta t}{C} \sum_{j=1}^{k-1} Q^{(j)} \mathrm{e}^{\frac{(j-k)\delta t}{R_d C}} - Q^{(k-1)} \frac{L}{\delta t} + Q^{(k)} \left(\frac{\delta t}{2C} + R_p + \frac{L}{\delta t} \right), \tag{3.15}$$

is based on an implicit formulation and where unconditional stability has been demonstrated [40]. Finally, we split the scheme in between its implicit and explicit parts

$$d_{\text{imp}}(\mathbf{u}, \mathbf{v}) = \left(\frac{\delta t}{2C} + R_p + \frac{L}{\delta t} \right) \int_\Gamma \mathbf{u} \cdot \mathbf{n} \, \mathrm{d}s \int_\Gamma \mathbf{v} \cdot \mathbf{n} \, \mathrm{d}s, \tag{3.16}$$

$$d_{\text{exp}}^{(k)}(\mathbf{v}) = \left(Q^{(0)} \mathrm{e}^{\frac{-t^{(k)}}{R_d C}} \left(\frac{\delta t}{2C} + R_d \right) + \frac{\delta t}{C} \sum_{j=1}^{k-1} Q^{(j)} \mathrm{e}^{\frac{(j-k)\delta t}{R_d C}} - Q^{(k-1)} \frac{L}{\delta t} \right) \int_\Gamma \mathbf{v} \cdot \mathbf{n} \, \mathrm{d}s, \tag{3.17}$$

in order to inject it in the variational formulation.

3.3. Numerical approximation

In the case of CFD approximations, we need to choose carefully the couple of approximation spaces velocity-pressure to ensure the compatibility with the *inf-sup* stability condition [41, 42]. A typical set of admissible couples is $\mathbb{P}_h^{k+1} - \mathbb{P}_h^k$ finite elements with $k \geq 1$. For $k = 1$, it gives the well-known Taylor-Hood finite elements couple $\mathbb{P}_h^2 - \mathbb{P}_h^1$. We thus consider the approximation space $V_h = \{\mathbf{v} \in (\mathbb{P}_h^2)^d \mid \mathbf{v}_{|\Gamma_{\text{Dir}}} = \mathbf{0}\}$ for the velocity field and $Q_h = \mathbb{P}_h^1$ for the pressure field. These approximation spaces are spanned by their respective finite element basis denoted $V_h = \text{span}(\psi_1, \ldots, \psi_{d\mathcal{N}_2})$ and $Q_h = \text{span}(\varphi_1, \ldots, \varphi_{\mathcal{N}_1})$. Injecting these basis of V_h and Q_h in the bilinear forms (3.6), (3.7), (3.8) and (3.9), we respectively obtain: the stiffness matrix $\mathbb{A}_h \in \mathbb{R}^{d\mathcal{N}_2 \times d\mathcal{N}_2}$ given by $(\mathbb{A}_h)_{ij} = a(\psi_i, \psi_j)$, $1 \leq i, j \leq d\mathcal{N}_2$; the divergence matrix $\mathbb{B}_h \in \mathbb{R}^{\mathcal{N}_1 \times d\mathcal{N}_2}$ given by $(\mathbb{B}_h)_{ij} = b(\varphi_i, \psi_j)$, $1 \leq i \leq \mathcal{N}_1, 1 \leq j \leq d\mathcal{N}_2$; the mass matrix $\mathbb{C}_h \in \mathbb{R}^{d\mathcal{N}_2 \times d\mathcal{N}_2}$ given by $(\mathbb{C}_h)_{ij} = c(\psi_i, \psi_j)$, $1 \leq i, j \leq d\mathcal{N}_2$; and the Windkessel matrix $\mathbb{D}_h \in \mathbb{R}^{d\mathcal{N}_2 \times d\mathcal{N}_2}$ given by $(\mathbb{D}_h)_{ij} = d_{\text{imp}}(\psi_i, \psi_j)$, $1 \leq i, j \leq d\mathcal{N}_2$.

Assuming that the initial state $(\mathbf{u}_h^{(0)}, p_h^{(0)})$ is known, where the sub-index h denotes the numerical approximation, we want to compute $(\mathbf{u}_h^{(k)}, p_h^{(k)})$ for $k = 1, \ldots, K$. The algebraic formulation associated to the variational problem (3.5) is a linear system of dimension $d\mathcal{N}_2 + \mathcal{N}_1$ given by

$$\begin{bmatrix} \mathbb{C}_h + \mathbb{A}_h + \mathbb{D}_h & \mathbb{B}_h^t \\ \mathbb{B}_h & \mathbb{O} \end{bmatrix} \begin{bmatrix} \mathbf{u}_h^{(k+1)} \\ p_h^{(k+1)} \end{bmatrix} = \begin{bmatrix} d_{\text{exp}}^{(k+1)} \left(\{\mathbf{u}_h^{(i)}\}_{i=0}^k \right) + \mathbb{C}_h \mathbf{u}_h^{(k)} \\ \mathbf{0} \end{bmatrix}. \tag{3.18}$$

Solving the whole problem then requires to solve K times this linear system. This task is achieved with parallel computing using in-house codes implemented with FreeFEM [43] and that have been validated beforehand by manufactured solutions and physical test cases.

4. Numerical results

Simulation results are presented for the two subjects described in the previous sections, namely T2 and T6. The computational meshes we use are composed of 326 349 tetrahedra for T2 and 221 971 for T6, respectively leading to 1 471 590 and 1 051 657 degrees of freedom. After running validation simulations to ensure convergence of the numerical results w.r.t. both time and space steps, we choose to use $K^{\text{cycle}} = 801$ time step per cycle, over 3 simulated cycles. It gives a total of $K = 2(K^{\text{cycle}} - 1) + K^{\text{cycle}} = 2\,401$ time steps to compute. The flow rates of the SSS and the StS obtained in Section 2.3 are used as inputs for the model. Two Windkessel

TABLE 3. Ranges of admissible resistances for T2.

Resistance	Min	Max
$R_{\text{eq},1}$	1.18×10^{-4}	1.26×10^{-4}
$R_{\text{eq},2}$	1.84×10^{-4}	2.08×10^{-4}

TABLE 4. Ranges of admissible resistances for T6.

Resistance	Min	Max
$R_{\text{eq},1}$	2.27×10^{-4}	2.55×10^{-4}
$R_{\text{eq},2}$	1.34×10^{-4}	1.70×10^{-4}

sub-models are attached to the model outlets, corresponding to right and left jugular levels. The flow rates of the RTS and the LTS are used to adjust the parameters of these Windkessel models by comparing them to the model outputs. Although our outlets are located at the jugular level, we choose to adjust them to transverse sinuses flow rates since the jugulars are outside the hypotheses of our model (See the limit in Fig. 2). Indeed, jugulars are extra-cranial and elastic, even collapsible, they can not be considered as rigid pipes. It is therefore unlikely that the model will be able to reproduce correctly these flow rates. It is important to remark here that the parameters associated to the Windkessel models depend implicitly on the inlets used.

4.1. Effect of the equivalent resistance in Windkessel models

A systematic method to adjust the equivalent resistance $R_{\text{eq}} = R_p + R_d$ of each of the Windkessel model is to observe the average flow rate and pressure over a cardiac cycle, they read

$$\overline{Q} = \frac{1}{T^{\text{cycle}}} \int_0^{T^{\text{cycle}}} Q(\tau)\, \mathrm{d}\tau \simeq \frac{1}{T^{\text{cycle}}} \sum_{k=0}^{K^{\text{cycle}}} \delta t\; Q(t^{(k)}) = \frac{1}{K^{\text{cycle}} - 1} \sum_{k=0}^{K^{\text{cycle}}} Q(t^{(k)}), \tag{4.1}$$

$$\overline{P} = \frac{1}{T^{\text{cycle}}} \int_0^{T^{\text{cycle}}} P(\tau)\, \mathrm{d}\tau \simeq \frac{1}{T^{\text{cycle}}} \sum_{k=0}^{K^{\text{cycle}}} \delta t\; P(t^{(k)}) = \frac{1}{K^{\text{cycle}} - 1} \sum_{k=0}^{K^{\text{cycle}}} P(t^{(k)}), \tag{4.2}$$

where T^{cycle} is the cardiac cycle duration. Using a specific regression described in Appendix A and based on 9 simulations, we are able to build the maps of average flow rate and pressure at the right outlet with respect to right and left equivalent resistances. The maps obtained are presented in Figure 7 and they allow us to infer ranges of the admissible resistances by setting a target flow rate, *i.e.* the RTS one, and a pressure target of 7.5(mmHg), corresponding to an healthy subject ICP in literature [44]. The ranges we obtained following this procedure are presented in Table 3 and Table 4.

4.2. Compliance and inertance tuning

To obtain numerical simulations better fitted with the real data, we can tune the compliances and inertances, and with the use of several indexes such as the amplitude, we are able to sort and retain the best parameter sets. However, tuning the compliance and inertance of each Windkessel model with systematic methods based on regression of these indexes is less adapted than for the resistances case, as they interfere one with the other. It is then necessary to use more elaborated data assimilation methods, which represents an ongoing work.

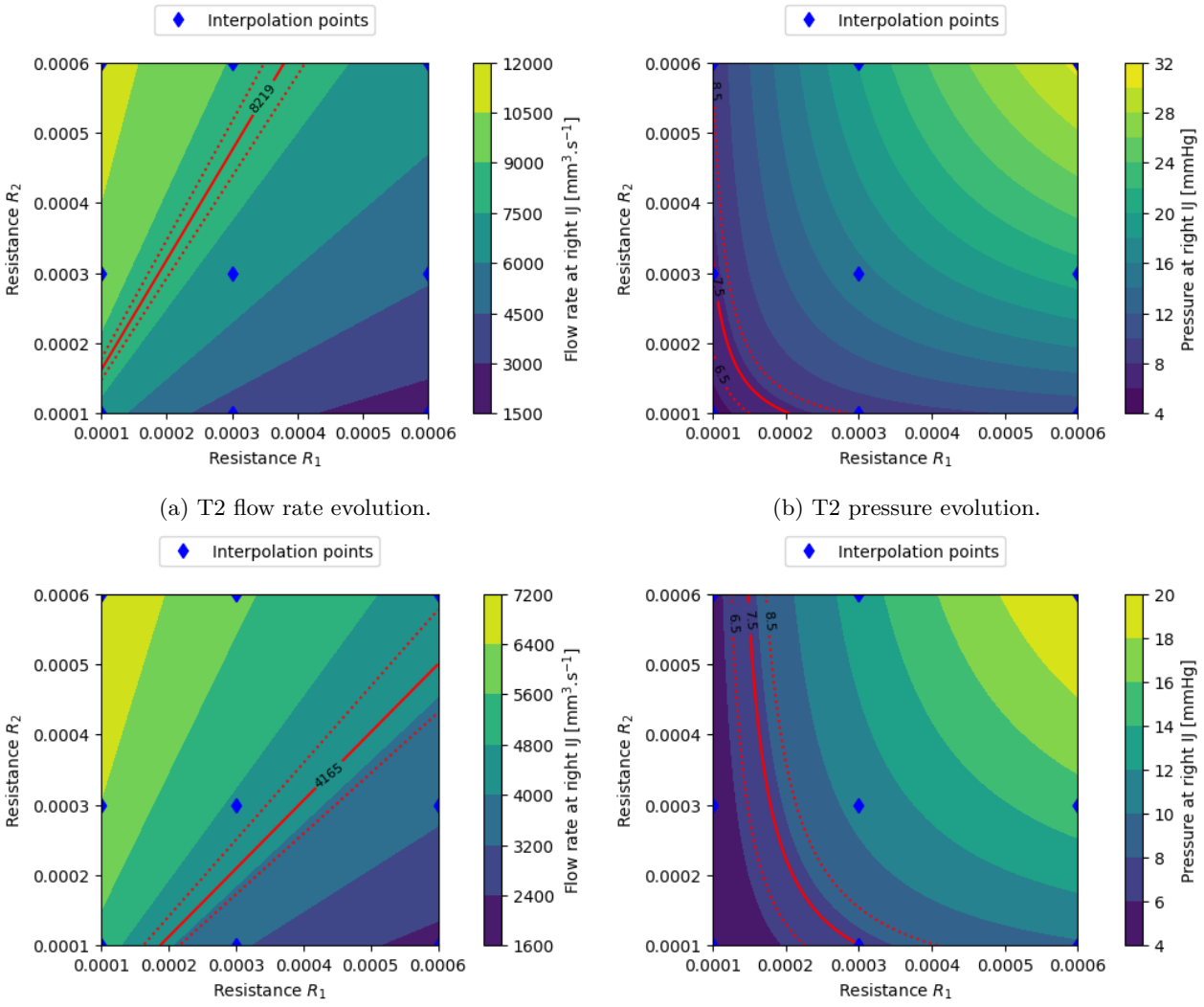

(a) T2 flow rate evolution.

(b) T2 pressure evolution.

(c) T6 flow rate evolution.

(d) T6 pressure evolution.

FIGURE 7. Interpolant of the field of flow rate and pressure evolution at the right outlet with respect to the equivalent resistance of the Windkessel models (9 simulations used as interpolation points).

After an empirical exploration and in order to illustrate our model performance, we ran 4 simulations with the parameter sets presented in Table 5 for T2 and in Table 6 for T6. The equivalent resistance is distributed between the proximal and the distal resistances with respectively 1/10 and 9/10 ratio. In Figures. 8a, 8b, 9a and 9b we compare the flow rates obtained at the outlets of the model with the measurements of the transverse sinuses from the PC-MRI acquisitions. We observe that the simulated flow rates are relatively close to the measured ones, meaning that the numerical model is able to reproduce the main features of the velocity field. Thus, we can consider this velocity field extended by the model to the whole domain to infer quantities of interest with high confidence. In Figures 8c, 8d, 9c and 9d we display the pressure found at the outlets and for which we do not have measurements to compare with. Although the mean pressure is prescribed at the outlets by the equivalent resistances of the Windkessel models, the pressure drop and the pressure variations

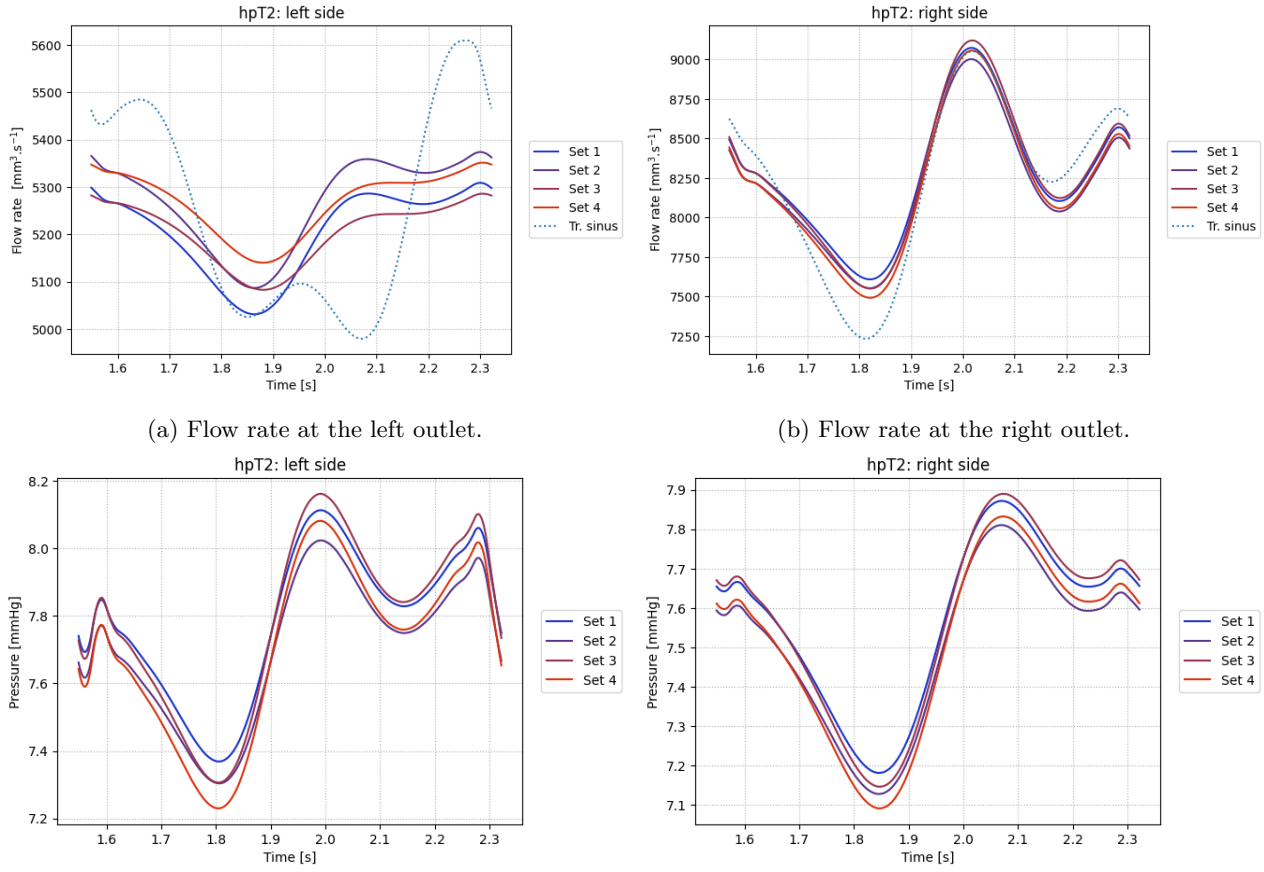

(a) Flow rate at the left outlet.

(b) Flow rate at the right outlet.

(c) Pressure at the left outlet.

(d) Pressure at the right outlet.

FIGURE 8. Simulation for T6 with parameter sets matching the flow rate evolution, see Table 5.

TABLE 5. Sets of parameters for accurate simulations T2 case.

T2	$R_{p,1}$	$R_{d,1}$	C_1	L_1	$R_{p,2}$	$R_{d,2}$	C_2	L_2
Set 1	1.22×10^{-5}	1.10×10^{-4}	10^3	1×10^{-6}	1.95×10^{-5}	1.75×10^{-4}	10^1	2.5×10^{-5}
Set 2	1.22×10^{-5}	1.10×10^{-4}	10^3	1×10^{-6}	1.95×10^{-5}	1.75×10^{-4}	10^2	2.5×10^{-5}
Set 3	1.22×10^{-5}	1.10×10^{-4}	10^3	1×10^{-6}	1.95×10^{-5}	1.75×10^{-4}	10^1	5×10^{-5}
Set 4	1.22×10^{-5}	1.10×10^{-4}	10^3	1×10^{-6}	1.95×10^{-5}	1.75×10^{-4}	10^2	5×10^{-5}

are fully computed by the numerical model, and yet gives an information not accessible otherwise. We observe in Figure 9 that despite the flow rates associated to the 4 parameter sets are close to the measurements, the pressure field can show different behaviors. It follows that without any extra information regarding the pressure, beside the physiological values in literature, it is not possible to obtain a unique pattern for the pressure field. Finally, in Figures 10 and 11, we show streamlines of the flow to illustrate its complexity and the presence of local 3-dimensional effects that should be taken into account when this system is studied. The pressure field is also presented to illustrate the variation between right and left sides of the network.

TABLE 6. Sets of parameters for accurate simulations T6 case.

T6	$R_{p,1}$	$R_{d,1}$	C_1	L_1	$R_{p,2}$	$R_{d,2}$	C_2	L_2
Set 1	2.40×10^{-5}	2.16×10^{-4}	10^1	1×10^{-6}	1.51×10^{-5}	1.36×10^{-4}	10^2	1×10^{-6}
Set 2	2.40×10^{-5}	2.16×10^{-4}	10^1	5×10^{-5}	1.51×10^{-5}	1.36×10^{-4}	10^2	5×10^{-5}
Set 3	2.40×10^{-5}	2.16×10^{-4}	10^2	1×10^{-6}	1.51×10^{-5}	1.36×10^{-4}	10^3	1×10^{-6}
Set 4	2.40×10^{-5}	2.16×10^{-4}	10^2	5×10^{-5}	1.51×10^{-5}	1.36×10^{-4}	10^3	5×10^{-5}

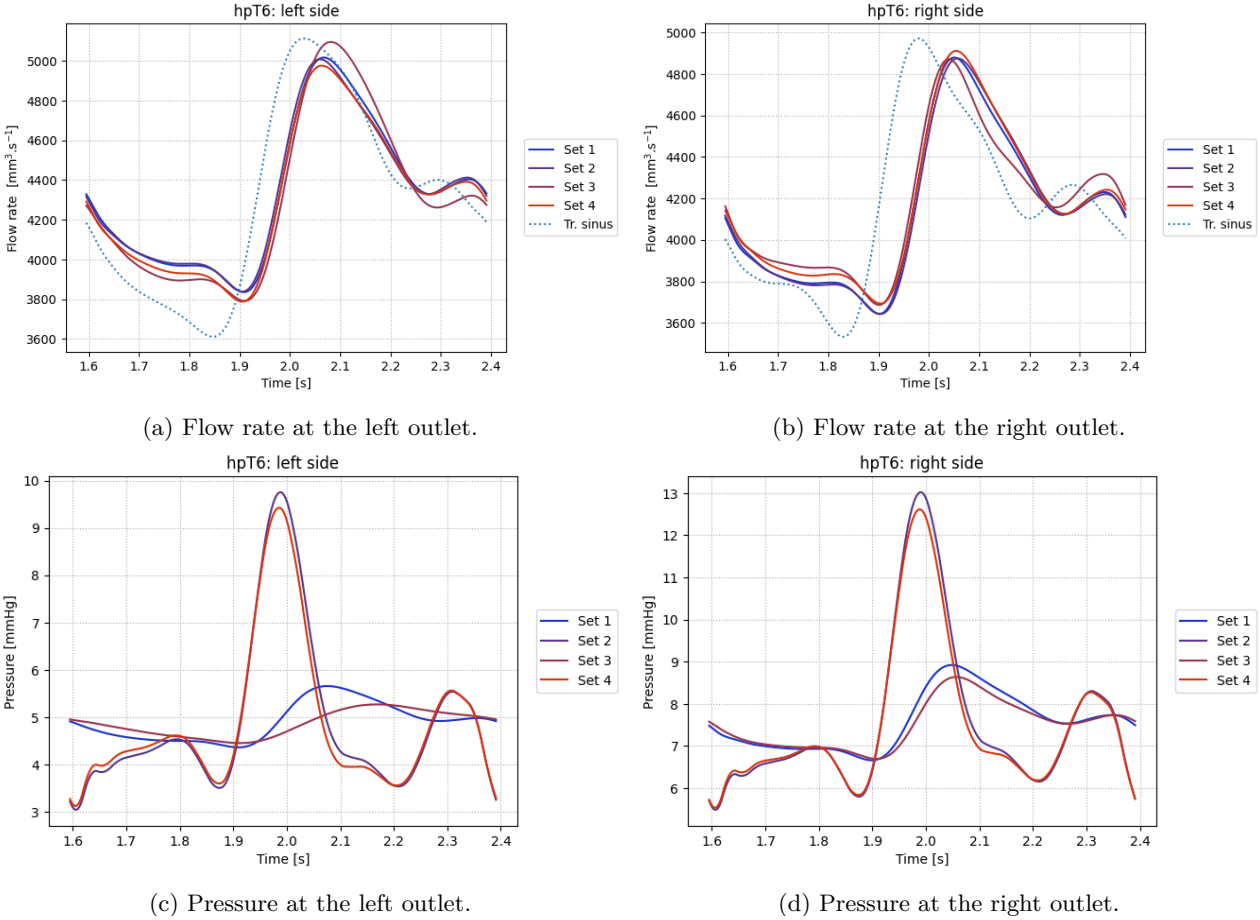

(a) Flow rate at the left outlet.

(b) Flow rate at the right outlet.

(c) Pressure at the left outlet.

(d) Pressure at the right outlet.

FIGURE 9. Simulation for T6 with parameter sets matching the flow rate evolution, see Table 6.

4.3. Discussion

Before going into the details of the results, we point out that one main limitation of the current numerical model is its computational cost. The choice of the linearization using the characteristics method is adapted to the situation as it tends to be very stable in the vascular simulation context [45], and allows to use efficient algorithms in back-end. However this method is hardly scalable in a parallel computing paradigm and leads to sub-optimal performances. In the current state of our code we limit the computation to 4 cores, resulting in 10 to 12 hours per simulations. Changing the methods used, and hence the corresponding code, to improve computational efficiency while maintaining the confidence in the outputs represent an ongoing work.

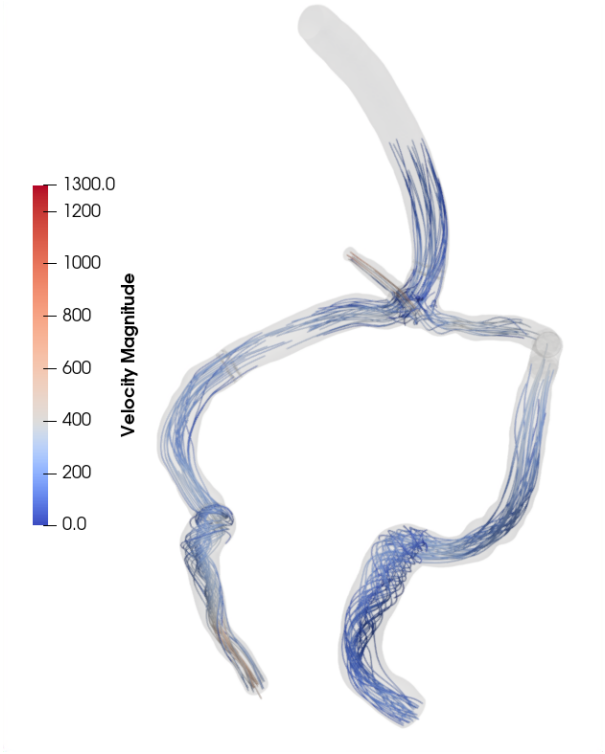

(a) Streamlines of the velocity field.

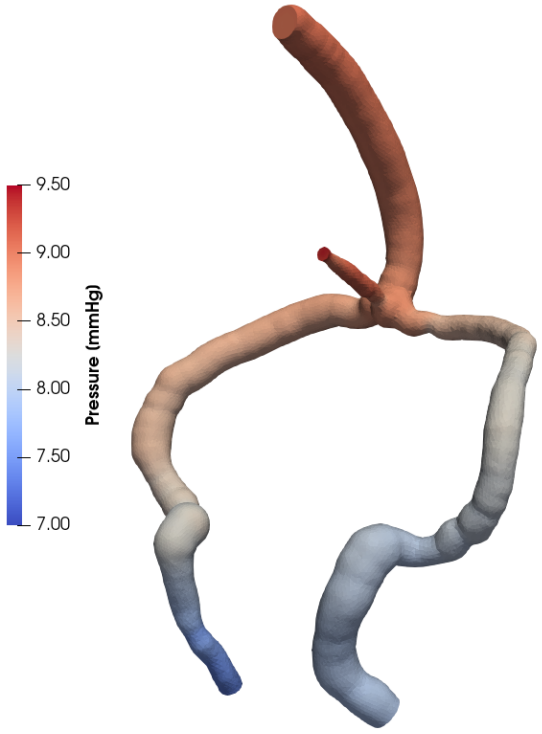

(b) Pressure field.

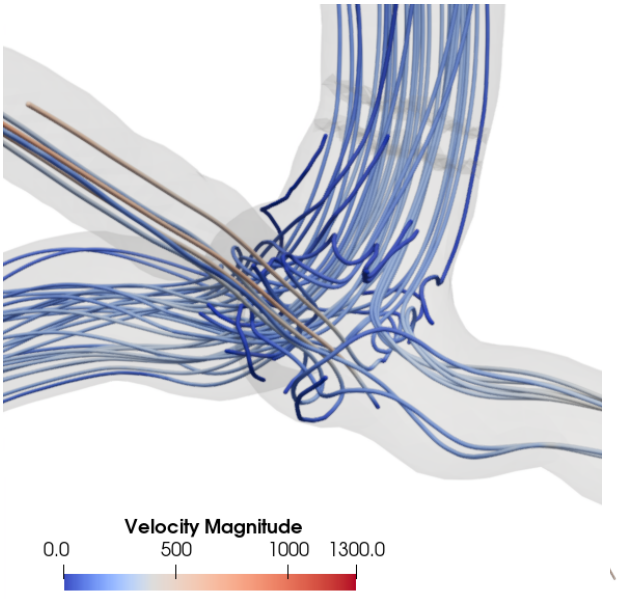

(c) Zoom on the streamlines at the sinus confluence.

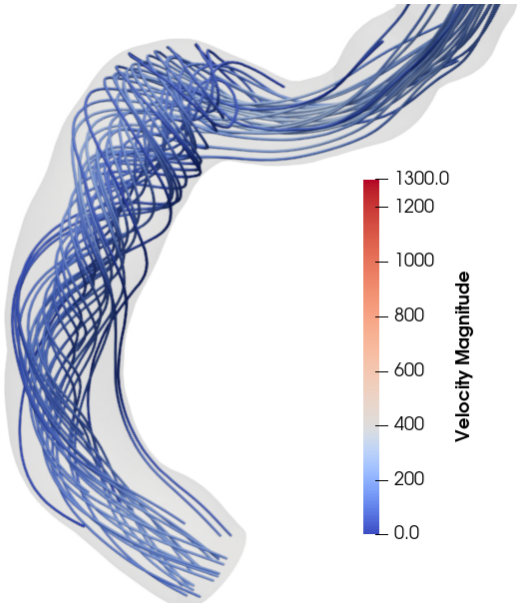

(d) Zoom on streamlines at the left transverse sinus.

FIGURE 10. Simulation results for T2 with parameter set 1 from Table 5.

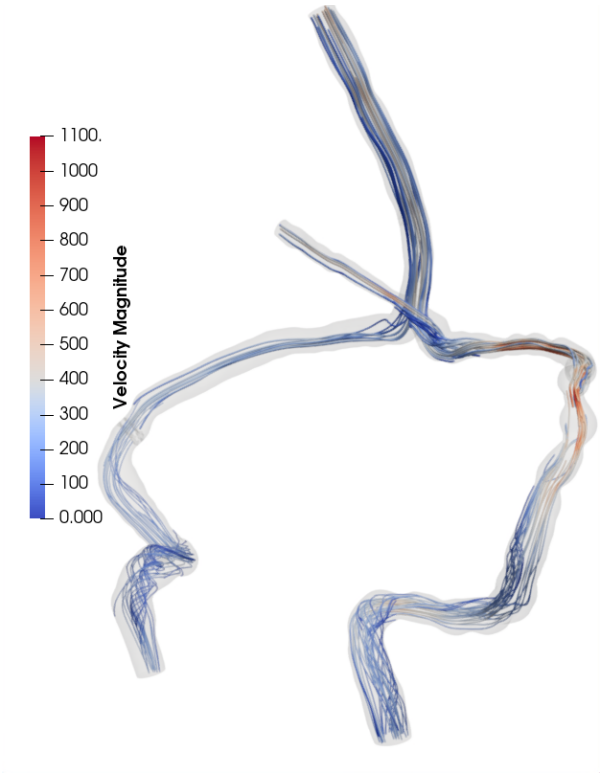

(a) Streamlines of the velocity field.

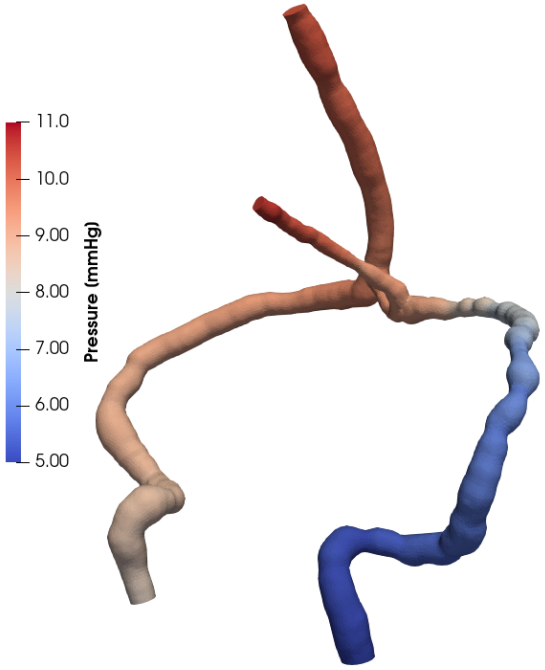

(b) Pressure field.

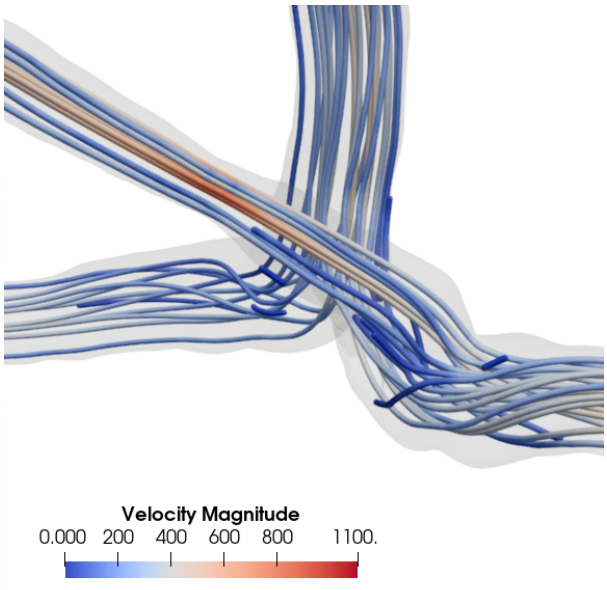

(c) Zoom on the streamlines at the sinus confluence.

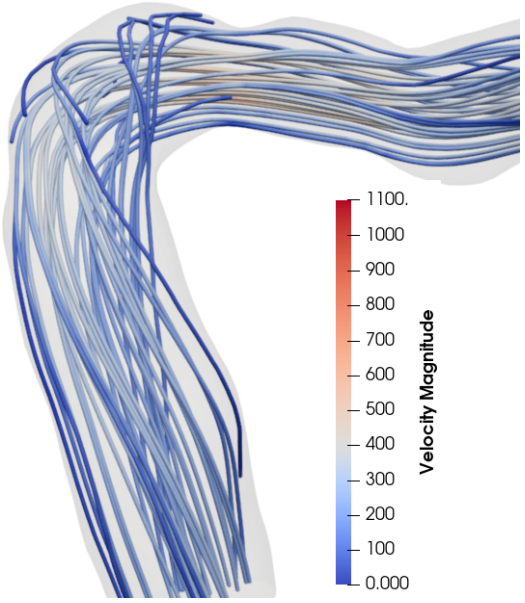

(d) Zoom on streamlines at the left transverse sinus.

FIGURE 11. Simulation results for T6 with parameter set 1 from Table 6.

Results for T2 and T6 are quite different, not only because of the geometry but also because of the flow ratio between right and left. In both cases, we are able to adjust the resistances in such a way that the mean value of the flow rate on the one hand, and of the pressure on the other hand, match the provided values. However tuning the compliance and inertance parameters with systematic methods based on regression is not possible and yet represent a challenging task, even in this simple configuration. Sophisticated data assimilation methods must be considered at this point to make this parameter research tractable before proposing extension of the current model. Nevertheless, it appears that the values we obtained empirically are close to those one can find in the literature [46, 47]. It is noticeable that at the jugular level, the model outputs are far from the measurements, which is acceptable at the moment, since jugulars are outside hypotheses of the model. Although the pressure cannot be set with certainty, the overall shape of the pressure curve seems fairly close to what is usually observed, *i.e.* several peaks with a larger one at first. The next step regarding this issue is to work on patients where the pressure is invasively measured, in order to calibrate our parameters much better.

We made some choices to find acceptable parameters that can be discussed. As we also have access to the arterial input at the cervical level (C2-C3, see slice *PCV60cervasc* in Fig. 3), we could have chosen to use the value of the total arterial flow as the reference volume for the venous network. But as it have been already stated, lots of vessels are neglected in our model and this would have led to large values to drain outside the cerebral compartment, which is not realistic. Finally, we observe that there is a phase shift in between model outputs and measurements (*e.g.* in Figs. 9a and 9d). The latter cannot be reproduced by the numerical model due to the fluid incompressibility and the rigid structure hypotheses. Hence, this phase shift can be done asymmetrically, by forcing the flow to go on one side *via* the Windkessel models, but not on both sides at the same time.

Extracting an accurate geometry of the vascular network is a critical point, as it directly impacts the simulated fluid flow. For example, if a segment of the mesh is artificially narrowed during the image processing, it will lead to an over-amplification of the pressure. Meanwhile, the final geometry must also be smooth enough to ensure that the mesh built upon it will be conform, and hence, suitable for simulation, while avoiding the introduction of non-realistic vortices. All these constraints motivate the choice of the centerline approach used here, despite the introduction of relatively circular sections. Indeed, even if this approach seems well adapted for arteries, it is not really suited for veins and sinuses as their sections are rarely this shape. However, it provides some starting point to deal with realistic meshes needed for the rest of the study. Efforts are currently made to circumvent this limitation by recording additional information, such as three radii for triangular sections often encountered in sinuses. Further work has to be done to estimate the impact of such circular approximations of triangular sections regarding the current framework. It is also noticeable that the overall geometric accuracy of the derived mesh is clearly influenced by the choice of segmentation methods. However, this task can hardly be automatized, due to the wide subject variability of the venous network and the presence of other vessels almost indistinguishable from those of interest. It follows that obtaining an acceptable computational mesh is a time-consuming process and it makes the sensitivity analysis with respect to the geometry difficult at the moment. Nevertheless, our assessment is that the average cumulative error at wall level remains within an acceptable range in comparison to the image errors inherent to the MRI acquisition technique used in the current study.

5. Conclusion

Excluding the software *flow* provided by the CHIMERE team, all steps of the current data processing chain have been developed in order to provide a fully accessible, reusable and open source framework [48].

To be in accordance with the physiology, we have shown that data of the specific subject must be used. To this end, we developed processes to extract structural data from MRI as well as physiological measurements from PC-MRI of the same subject. Due to the wide inter-individual variability of the cerebral venous network, those tasks can essentially not be automatized, we however implemented them in the most standardized manner. We also provided a methodology to integrate these individual-specific data into our numerical model under certain arguable choices and hypotheses. Almost all the available information is used in this context, either as an input (mesh, boundary condition) or as a control for outputs (flow rates). Using comparison between real data and these control measurements, we were able to adjust the parameters of our model, up to some extent. The values

obtained for these parameters look reasonable in regard of the literature and tends to prove that the numerical model captures the essence of the physics behind.

In addition, we have shown here that geometry is not the only data needed to make the model reproduce a physiological behavior. Windkessel models seem mandatory to take into account the neglected part of the venous network, and especially its structural component, while keeping computations tractable. In the meantime, we have to find acceptable sets for the parameters associated to these Windkessel sub-models and we have shown that this represents a challenging task. The parameters calibration proposed here is only empirical and based on qualitative observations. The main purpose of this work is rather to confirm that coupling between real data and numerical model is necessary to obtain reliable physiological behaviors, than to provide quantitative results yet. The current numerical model gives already encouraging results, even if the outputs we obtain do not fit perfectly the real measurements. The quantitative aspect requires a detailed exploration of the model, and especially the effects of each input parameters, and represents an ongoing work.

Furthermore, several possible extensions of the current model have been proposed through this paper and each of them should be considered carefully. At first, in a new incoming type of acquisition, the data will contain the whole flow rate information over multiple cardiac cycles and will pave the way for uncertainty quantification of the model. The goal is to keep an accurate, and yet understandable, numerical model. One last issue we address in the results discussion is the lack of information regarding the pressure. The former purpose of such model was to provide, at least, quantitative information on the pressure using only flow rates data and this task is fulfilled. However, the model still have to be calibrated to make this pressure information reliable, using for instance patient for whom the pressure is recorded invasively. Once this has been achieved, the model can be used to infer de-regulations of the cerebral venous system in pathological cases such as idiopathic high ICP.

Funding

This work was founded by the French national research agency (ANR) for the Human and Animal NUmerical Models for the crANio-spinal system (HANUMAN) project ANR-18-CE45-0014[3].

Data availability statement

The research data and code associated with this article are available in Zenodo https://zenodo.org/records/11032278 [48].

References

[1] M. Aletti, J.-F. Gerbeau and D. Lombardi, A simplified fluid–structure model for arterial flow. Application to retinal hemodynamics. *Comput. Methods Appl. Mech. Eng.* **306** (2016) 77–94.

[2] P. Chen, A. Quarteroni and G. Rozza, Simulation-based uncertainty quantification of human arterial network hemodynamics. *Int. J. Numer. Methods Biomed. Eng.* **29** (2013) 698–721.

[3] L. Formaggia, D. Lamponi and A. Quarteroni, One-dimensional models for blood flow in arteries. *J. Eng. Math.* **47** (2003) 251–276.

[4] R. Torii, M. Oshima, T. Kobayashi, K. Takagi and T.E. Tezduyar, Fluid–structure interaction modeling of blood flow and cerebral aneurysm: significance of artery and aneurysm shapes. *Comput. Methods Appl. Mech. Eng.* **198** (2009) 3613–3621.

[5] O. Miraucourt, S. Salmon, M. Szopos and M. Thiriet, Blood flow in the cerebral venous system: modeling and simulation. *Comput. Methods Biomech. Biomed. Eng.* **20** (2017) 471–482.

[6] P. Mollo, *Développement et analyse du modèle numérique du système crânio-spinal*, these de doctorat, Reims (2023).

[7] L.O. Müller and E.F. Toro, Enhanced global mathematical model for studying cerebral venous blood flow. *J. Biomech.* **47** (2014) 3361–3372.

[8] V.M. Pereira, N.M. Cancelliere, M. Najafi, D. MacDonald, T. Natarajan, I. Radovanovic, T. Krings, J. Rutka, P. Nicholson and D.A. Steinman, Torrents of torment: turbulence as a mechanism of pulsatile tinnitus secondary to venous stenosis revealed by high-fidelity computational fluid dynamics. *J. Neurointerv. Surg.* **13** (2021) 732–737.

[9] E.F. Toro, M. Celant, Q. Zhang, C. Contarino, N. Agarwal, A. Linninger and L.O. Müller, Cerebrospinal fluid dynamics coupled to the global circulation in holistic setting: mathematical models, numerical methods and applications. *Int. J. Numer. Methods Biomed. Eng.* **38** (2022) e3532.

[3] https://anr.fr/Projet-ANR-18-CE45-0014

[10] S. Stoquart-ElSankari, P. Lehmann, A. Villette, M. Czosnyka, M.-E. Meyer, H. Deramond and O. Balédent, A phase-contrast MRI study of physiologic cerebral venous flow. *J. Cerebral Blood Flow Metab.* **29** (2009) 1208–1215. Publisher: SAGE Publications Ltd STM.

[11] B. Mokri, The Monro–Kellie hypothesis. *Neurology* **56** (2001) 1746–1748.

[12] M.H. Wilson, Monro-Kellie 2.0: the dynamic vascular and venous pathophysiological components of intracranial pressure. *J. Cerebral Blood Flow Metab.* **36** (2016) 1338–1350.

[13] M. Nedergaard and S.A. Goldman, Glymphatic failure as a final common pathway to dementia. *Science (New York, N.Y.)* **370** (2020) 50–56.

[14] M.-Y. Jaffrin and F. Goubel, Biomécanique des fluides et des tissus. Masson, Paris Milan Barcelone (1998).

[15] N. Alperin, S.H. Lee, A. Sivaramakrishnan and S.G. Hushek, Quantifying the effect of posture on intracranial physiology in humans by MRI flow studies. *J. Magn. Resonance Imaging* **22** (2005) 591–596.

[16] P. Liu, S. Fall and O. Balédent, Use of real-time phase-contrast MRI to quantify the effect of spontaneous breathing on the cerebral arteries. *NeuroImage* **258** (2022) 119361.

[17] M. Prokop, H.O. Shin, A. Schanz and C.M. Schaefer-Prokop, Use of maximum intensity projections in CT angiography: a basic review. *Radiographics* **17** (1997) 433–451.

[18] G. Pagé, Quantification et caractérisation des écoulements sanguins dans l'arborescence vasculaire de la région cervico-faciale par Imagerie par Résonance Magnétique de flux: évaluation et application, these de doctorat, Amiens (2016).

[19] G.L. Streeter, The development of the venous sinuses of the duramater in the human embryo. *Am. J. Anat.* **18** (1915) 145–178.

[20] J.M Das and Y. Al Khalili, Jugular Foramen Syndrome, in StatPearls. StatPearls Publishing, Treasure Island (FL) (2023).

[21] H.K. Park, H.G. Bae, S.K. Choi, J.C. Chang, S.J. Cho, B.J. Byun and K.B. Sim, Morphological study of sinus flow in the confluence of sinuses. *Clin. Anat.* **21** (2008) 294–300.

[22] V. Chabannes, A. Ancel, J. Jomier and C. Prud'Homme, AngioTK: An Open Platform to reconstruct vessels from MRI images and simulate blood flows to ultimately provide Virtual Angiographies. Rencontre Inria Industrie Santé (2015).

[23] O. Merveille, B. Naegel, H. Talbot, L. Najman and N. Passat, 2D filtering of curvilinear structures by ranking the orientation responses of path operators (RORPO). *Image Process. Line* **7** (2017) 246–261.

[24] J. Lamy, O. Merveille, B. Kerautret, N. Passat and A. Vacavant, Vesselness filters: a survey with benchmarks applied to liver imaging, in International Conference on Pattern Recognition (ICPR). Milan, Italy (2020) 3528–3535.

[25] A. Fedorov, R. Beichel, J. Kalpathy-Cramer, J. Finet, J.-C. Fillion-Robin, S. Pujol, C. Bauer, D. Jennings, F. Fennessy, M. Sonka, J. Buatti, S. Aylward, J.V. Miller, S. Pieper and R. Kikinis, 3D Slicer as an image computing platform for the quantitative imaging network. *Magn. Reson. Imaging* **30** (2012) 1323–1341.

[26] L. Antiga, M. Piccinelli, L. Botti, B. Ene-Iordache, A. Remuzzi and D.A. Steinman, An image-based modeling framework for patient-specific computational hemodynamics. *Med. Biol. Eng. Comput.* **46** (2008) 1097–1112.

[27] R. Izzo, D. Steinman, S. Manini and L. Antiga, The vascular modeling toolkit: a python library for the analysis of tubular structures in medical images. *J. Open Source Softw.* **3** (2018) 745.

[28] L.O. Müller and E.F. Toro, A global multiscale mathematical model for the human circulation with emphasis on the venous system. *Int. J. Numer. Methods Biomed. Eng.* **30** (2014) 681–725.

[29] G. Taubin *et al.*, Linear anisotropic mesh filtering. *Res. Rep. RC22213 IBM* **1** (2001).

[30] C. Geuzaine and J.-F. Remacle, Gmsh: A 3-D finite element mesh generator with built-in pre-and post-processing facilities. *Int. J. Numer. Methods Eng.* **79** (2009) 1309–1331.

[31] G. Balarac, F. Basile, P. Bénard, F. Bordeu, J.-B. Chapelier, L. Cirrottola, G. Caumon, C. Dapogny, P. Frey, A. Froehly, G. Ghigliotti, R. Laraufie, G. Lartigue, C. Legentil, R. Mercier, V. Moureau, C. Nardoni, S. Pertant and M. Zakari, Tetrahedral remeshing in the context of large-scale numerical simulation and high performance computing. *Math. Action* **11** (2022) 129–164.

[32] C. Dapogny, C. Dobrzynski and P. Frey, Three-dimensional adaptive domain remeshing, implicit domain meshing, and applications to free and moving boundary problems. *J. Computat. Phys.* **262** (2014) 358–378.

[33] C. Dobrzynski and P. Frey, Anisotropic Delaunay mesh adaptation for unsteady simulations, in *17th international Meshing Roundtable, United States* (2008) 177–194.

[34] O. Balédent, M.-C. Henry-Feugeas and I. Idy-Peretti, Cerebrospinal fluid dynamics and relation with blood flow: a magnetic resonance study with semiautomated cerebrospinal fluid segmentation. *Invest. Radiol.* **36** (2001) 368–377.
[35] L. Formaggia, A. Quarteroni and A. Veneziani, eds., *Cardiovascular Mathematics*. Springer Milan, Milano (2009).
[36] M. Thiriet, Cell and tissue organization in the circulatory and ventilatory systems, Vol. 1 of *Biomathematical and Biomechanical Modeling of the Circulatory and Ventilatory Systems*. Springer (2011).
[37] M. Thiriet, Biology and Mechanics of Blood Flows. Springer, New York, NY (2008).
[38] O. Pironneau, On the transport-diffusion algorithm and its applications to the Navier–Stokes equations. *Numer. Math.* **38** (1982) 309–332.
[39] A. Quarteroni, Numerical Models for Differential Problems, Vol. 16 of *MS&A*. Springer International Publishing, Cham (2017).
[40] C. Grandmont and S. Martin, Existence of solutions and continuous and semi-discrete stability estimates for 3D/0D coupled systems modelling airflows and blood flows. *ESAIM: Math. Model. Numer. Anal.* **55** (2021) 2365–2419.
[41] F. Brezzi, On the existence, uniqueness and approximation of saddle-point problems arising from lagrangian multipliers. *ESAIM: Math. Model. Numer. Anal.* **8** (1974) 129–151.
[42] V. Girault and P.-A. Raviart, Finite Element Methods for Navier–Stokes Equations, Vol. 5 of *Springer Series in Computational Mathematics*. Springer Berlin Heidelberg, Berlin, Heidelberg (1986).
[43] F. Hecht, New development in FreeFem++. *J. Numer. Math.* **20** (2012) 251–265.
[44] J. Ekstedt, CSF hydrodynamic studies in man. 2. Normal hydrodynamic variables related to CSF pressure and flow. *J. Neurol. Neurosurg. Psychiatry* **41** (1978) 345–353.
[45] J. Fouchet-Incaux, Artificial boundaries and formulations for the incompressible Navier–Stokes equations: applications to air and blood flows. *SeMA J.* **64** (2014) 1–40.
[46] A.A. Domogo, P. Reinstrup and J.T. Ottesen, Mechanistic-mathematical modeling of intracranial pressure (ICP) profiles over a single heart cycle. The fundament of the ICP curve form. *J. Theor. Biol.* **564** (2023) 111451.
[47] M. Unnerbäck, J.T. Ottesen and P. Reinstrup, Validation of a mathematical model for understanding intracranial pressure curve morphology. *J. Clin. Monitor. Comput.* **34** (2020) 469–481.
[48] P. Mollo, G. Dollé, S. Salmon and O. Baledent, Accurate Cerebral Blood Flow Simulations Compare to Real Data MMNP (2025). https://doi.org/10.5281/zenodo.11032278.

Appendix A. Model for interpolation of the mean flow rate

We denote Q_{tot} the total flow rate (sum of right and left) and α the ratio between right and left. Considering the model simplification described in Figure A.1, we deduce

$$\begin{cases} \delta P_{\text{TR}} = \alpha Q_{\text{tot}} R_{\text{TR}} \\ \delta P_1 = \alpha Q_{\text{tot}} R_1 \\ \delta P_{\text{TL}} = (1-\alpha) Q_{\text{tot}} R_{\text{TL}} \\ \delta P_2 = (1-\alpha) Q_{\text{tot}} R_2 \\ \delta P = \delta P_{\text{TR}} + \delta P_1 \\ \delta P = \delta P_{\text{TL}} + \delta P_2 \end{cases}.$$

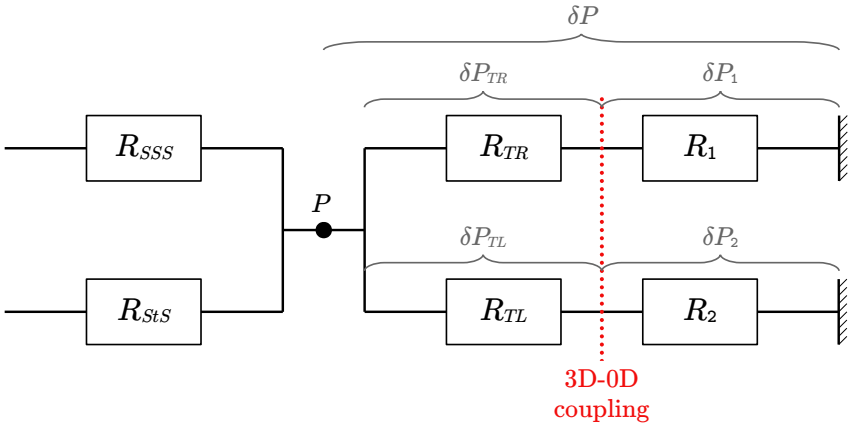

FIGURE A.1. Model simplification.

It follows that

$$\alpha Q_{\text{tot}} R_1 + \alpha Q_{\text{tot}} R_{\text{TR}} = (1-\alpha) Q_{\text{tot}} R_2 + (1-\alpha) Q_{\text{tot}} R_{\text{TL}}. \tag{A.1}$$

Since R_{TR} and R_{TL} are unknown, we can rewrite (A.1) as

$$\alpha = \frac{R_2 + R_{\text{TL}}}{R_1 + R_{\text{TR}} + R_2 + R_{\text{TL}}} = \frac{R_2 + a}{R_1 + R_2 + b}, \tag{A.2}$$

where a and b are to be defined. In order to define them, we can write (A.2) as

$$-a + \alpha b = R_2 - \alpha(R_1 + R_2) \tag{A.3}$$

and use a linear regression with at least two simulations results. The pressure at the right, resp. left, outlet of the 3D model corresponds to δP_1, resp. δP_2, they read

$$\delta P_1 = \frac{R_2 + a}{R_1 + R_2 + b} Q_{\text{tot}} R_1, \qquad \delta P_2 = \frac{R_2 + a}{R_1 + R_2 + b} Q_{\text{tot}} R_2. \tag{A.4}$$

Now, if we consider a target ratio α^* and a target pressure at the right outlet δP_1^*, we are looking for R_1, R_2 such that

$$\begin{cases} \frac{R_2+a}{R_1+R_2+b} Q_{\text{tot}} R_1 = \delta P_1^* \\ \frac{R_2+a}{R_1+R_2+b} = \alpha^* \end{cases},$$

the solution of the problem reads

$$\begin{cases} R_1 = \frac{\delta P_1^*}{Q_{\text{tot}} \alpha^*} \\ R_2 = \frac{1}{\alpha^* - 1} \left(a - \frac{\delta P_1^*}{Q_{\text{tot}}} - \alpha^* b \right) \end{cases}.$$